Zeolite/polymer core-shell hybrid nanoparticles with hierarchical micro/meso-pores

Rita Zakhia Douaihy, Houssein Nasrallah, Oleg Lebedev, Jaafar El Fallah, Rémy Guillet-Nicolas, Alexandre Vimont, Philippe Bazin, Mohamad El-Roz

New approach for preparing zeolite-polymer hybrid materials with hierarchical porosity

Rita Zakhia Douaihy [a], Houssein Nasrallah [a], Oleg Lebedev [b], Jaafar El Fallah [a], Rémy Guillet-Nicolas [a], Alexandre Vimont [a], Philippe Bazin [a,], Mohamad El-Roz [a,*]*

[a] Normandie Université, ENSICAEN, UNICAEN, CNRS, Laboratoire Catalyse et Spectrochimie, 14050 Caen, France

[b] Normandie Université, ENSICAEN, UNICAEN, CNRS, Laboratoire CRISMAT, 14050 Caen, France

[*] Corresponding authors: mohamad.elroz@ensicaen.fr; philippe.bazin@ensicaen.fr

KEYWORDS: hybrid materials, zeolites, polymer, core-shell, dehydration

ABSTRACT

Here, we report a new approach for preparing zeolite-polymer core-shell like materials with hierarchical porosity via photopolymerization of trifunctional acrylic monomer (TMPTA) under UV-visible irradiation, using bifunctional Silane-based PhotoInitiator (SPI-1) as coupling agent. The free radicals, generated on the surface of zeolites, initiate the polymerization of the diluted monomers and therefore create an external and mesoporous polymer shell layer. The efficiency of the photopolymerization process and the textural properties of synthesized materials are investigated using different techniques including PXRD, TGA, UV-Vis, FTIR, SEM and TEM. The accessibility to the pores of the zeolite core

are investigated by N_2 physisorption at 77 K and other probe molecules using IR spectroscopy. Interestingly, the new approach is highly repetitive and reproducible and the accessibility to the zeolite's micropores is preserved with around 90 %. The newly synthesized hybrid materials show modified adsorption/separation capacities compared to the parent material toward water and ethanol adsorptions and during the dehydration of ethanol.

INTRODUCTION

In the last decades, mixed matrix membranes (MMMs) emerged to be excellent alternatives for polymeric and inorganic membranes[1, 2]. This is due to their outstanding performance that exceeds Robeson's upper bound for gas separation [3, 4]. Their importance arises from the combination of the selective separative and adsorptive characteristics of the inorganic porous fillers and the mechanical and economical properties of the polymer matrices[5]. Different porous materials including zeolites[6-8], silica nanoparticles[9], MOFs[10-12], COFs[13, 14], and others[15-17] were dispersed in the polymer matrix for gas separation[18-21], permeation and water/alcohol purification[7, 12, 22-24]. Despite the divers applications of MMMs, the heterogeneous dispersion of the inorganic filler, the accessibility to its pores, and the undesirable defect between the organic matrix and the inorganic particles in addition to the non-homogeneous coverage are the common limitations emanating during the their synthesis[1, 25]. To overcome these limitations, the polymer is treated either by its annealing above its glass transition temperature or by mixing it with a plasticizer to maintain its chain flexibility[22, 26]. The inorganic filler can be thermally treated, or its surface can be modified by coating or grafted with integral chain linkers and silane-based coupling agents to assure better dispersion and promote the adhesion to the polymer matrix[22, 27, 28]. Moreover, the synthesis procedures reported in the literature could be classified in the following three main approaches [29]: a) the polymer is added to a homogeneous suspension of inorganic particles, b) a predetermined quantity of inorganic particle is added to

a homogeneous suspension of the polymer, or c) separate homogeneous suspensions of polymer and inorganic particles are mixed together. Nevertheless, the limitations previously mentioned were not completely surpassed via these approaches. Therefore, extensive work has been imputed to improve the synthesis of MMMs via radical or cationic photopolymerization-based processes in the presence of a photoinitiator [30, 31].

Recently, a new approach has been validated by our group, where a MMM was synthesized by photopolymerization of an acrylate monomer on the surface of previously grafted silica nanoparticles with a silane-based photo-initiator [32-34]. Throughout this rapid and easy technique, and upon generation of free radicals on the surface of well-dispersed silica nanoparticles, a homogenous external layer of polymer is formed. The strong covalent bond between the silica particles and the polymer matrix resulted in a mixed membrane with enhanced mechanical properties. This synthesis procedure could be further conducted on other fillers such as zeolites. To the best of our knowledge, few works on the photopolymerization of monomers with zeolites as seedings for MMMs have been reported [35, 36]. However, some limitations have been encountered such as the effect of the Si/Al ratio on the efficiency of the polymerization and the accessibility to the zeolite micropores that was only accessible after calcination and deterioration of the polymer layer.

Thus, to surpass these limitations, we report here the synthesis of MFI-zeolite@polymer core-shell like structure, considered as a seeding for zeolite mixed matrix membrane. MFI nanoparticles are grafted with a previously synthesized silane-based photoiniator (SPI-1) by interactions between the silane groups of the zeolite and the ethoxy groups of the coupling agent. The grafted MFI nanoparticles are then tested in the free radical polymerization of diluted trimethylolpropane triacrylate (TMPTA). The obtained hybrid materials are then collected, purified and characterized using UV-Vis and IR spectroscopies and

thermogravimetric analyses. Their morphologies are examined using SEM and TEM. The accessibility of the micropores in the zeolite-polymer hybrid materials are investigated using N_2 sorption and adsorption of probe molecules. Finally, the newly synthesized and the parent materials are tested in the preferential adsorption of ethanol, water, and water/ethanol mixture, a highly desirable process for bio-ethanol dehydration. The preferential adsorption is considered as an efficient and energy saving approach for purification of this mixture, since ethanol is always collected in an aqueous mixture and cannot be used directly as a biofuel or additive to gasoline.

EXPERIMENTAL

Materials: Industrial H-MFI zeolites provided by Clariant (formerly Süd Chemie, Si/Al= 45) were used in this work without any further treatment. Isobutyrophenone (IBP, 97 %), Allyl bromide (99 %), Potassium t-butoxide (99.99 %), tert-butanol (≥ 99.5 %), Diethyl ether (99 %), Sodium sulfate (99.99 %), Triethoxysilane (95 %), Dodecane (≥ 99%), Pt/Al_2O_3 (5 wt%) and Trimethylolpropanetriacrylate (TMPTA) (technical grade) purchased from Aldrich, and Acetonitrile (AcN, 99 %) purchased from Alfa Aeasar, were used without any further purification.

Synthesis of 2,2-dimethyl-1-phenyl-5-(triethoxysilyl) pentane-1-one (SPI-1): The synthesis of SPI-1 is detailed in the supporting information (**Scheme S1** and **Figure S1**) and in reference 32.

Grafting of SPI-1 on the surface of the MFI zeolites (SPI-MFI): 1 g of MFI zeolites was dried at 150 °C and then dispersed in 10 mL of dodecane with 0.1 g of the previously synthesized SPI-1 under vigorous stirring for 20 minutes at 120 °C. The powder was collected by centrifugation and washed with acetonitrile (2 times) and several times with water and

ethanol to remove the excess of the ungrafted SPI-1 and the solvent. The final precipitate is dried using a freeze-dryer before characterization. This procedure was repeated at least three times to check the repetition of the process and the reproducibility of the results.

Photopolymerization efficiency:

The capacity and the efficiency of the grafted SPI-1 on zeolite were investigated using IR spectroscopy by following the kinetic of the C=C bond conversion of the TMPTA monomer. The conversion yield is calculated according to **equation 1**:

$$\boldsymbol{Conversion}\ (\%) = (\boldsymbol{A_0} - \boldsymbol{A_t})/\boldsymbol{A_0} * \mathbf{100} \qquad \textbf{(equation 1)}$$

where A_0 and A_t correspond to the band area of the characteristic C=C stretching band of TMPTA at 1635 cm^{-1} at t = 0 and t = time of the photopolymerization, respectively.

The photopolymerizable samples were prepared by mixing the 1 wt.% of SPI-1 (used as reference) or the grafted SPI-MFI (1.8 and 3.6 wt.%) with TMPTA monomer. Few drops of each mixture were spread on polypropylene films separated by a Teflon spacer (width = 100 μm and diameter = 2 cm^2), and subjected to monochromatic (LED 365 nm, Irradiance (306.4 mW/cm^2)) and polychromatic UV irradiations (Xe–Hg lamp (LC8-01A spotlight, Hamamatsu, L10852, 200 W, $I_0 \approx 150$ $mW.cm^{-2}$).

Preparation of MFI@Polymer:

40 mg of the previously grafted MFI zeolites were dispersed in 20 mL of acetonitrile (AcN) via sonication. 80 mg of the TMPTA monomer were added to the solution in a transparent reactor. The overall mixture was bubbled with argon under stirring for at least 15 minutes and then subjected to polychromatic irradiation for 15 minutes using a polychromatic Xe–Hg lamp (LC8-01A spotlight, Hamamatsu, L10852, 200 W, $I_0 \approx 150$ $mW.cm^{-2}$). The bubbling and the stirring were maintained throughout the irradiation. After polymerization, the white precipitate was collected by centrifugation. Then, the excess of the monomer and the solvent were

removed by washing with acetonitrile and water, respectively. The solid is then freeze-dried before characterization. The procedure was repeated at least three times to check the repetition of the process and the reproducibility of the results.

Characterization techniques:

The thermogravimetric analysis was recorded on a SETSYS analyzer (SETARAM) between 25 °C and 800 °C with a heating rate of 10 °C.min^{-1} under a flow of air (40 mL.min^{-1}).

UV-Vis measurements were performed with a Cary 4000 (Varian) spectrophotometer in the spectral range between 200 and 400 nm. The spectrophotometer is equipped with a Praying Mantis diffuse reflection accessory.

PXRD patterns are recorded on a PANalytical X'Pert Pro diffractometer with an average Cu Kα radiation (λ = 1.5418 Å). The θ-2θ scans are recorded in the range of 2θ between 5° and 50° and a step size ~ 0.0167.

Nitrogen sorption isotherms at 77K were recorded using a Micrometrics ASAP 2020 volumetric adsorption analyzer. Before the measurements, the samples were degassed under vacuum at 150 °C, 180 °C or 200 °C for 12 hours. The specific surface areas are determined from the BET equation following the procedure recommended by Rouquerol et al. for microporous sorbents[37]. The total pore volumes and the external surface areas are calculated from the *t*-plot method. Cumulative pore volume plots discussed in the SI were calculated via the VersaWin software 1.01 (Quantatec) using the adsorption branches of the isotherms and by applying the NLDFT kernel of (metastable) adsorption isotherms, considering an oxidic surface.

The morphologies of the parent and the modified samples were examined using electron microscopy. The SEM images were recorded using a TESCAN Mira field-emission scanning microscope at 20 kV. The TEM micrographs were recorded on a JEM200F cold FEG double aberration-corrected microscope equipped with a CENTURIO large-angle EDX detector. For

SEM, the powder was dispersed on a thin layer of tin, fixed on carbon tape and the MFI powder was coated with platinum. Before TEM, the powder was dispersed in ethanol on a holey carbon film and coated with copper.

The pore accessibility and their acidity are investigated by in-situ IR experiments of pyridine and collidine adsorption on a ~20 mg self-supported pellets of the pressed powder (10^7 Pa/cm^2, S = 2 cm^2). The spectra were recorded using an *in-situ* IR cell equipped with KBr windows connected to a Nicolet 6700 IR spectrophotometer, equipped with a DTGS detector and an extended-KBr beam splitter in the region between 400 and 5500 cm^{-1} (resolution 4 cm^{-1}, 128 scans)[38]. Before adsorption, MFI zeolites (MFI), MFI with grafted SPI-1 (SPI-MFI), and MFI with polymer (MFI@Polymer) were pretreated from room temperature to 150 °C (heating rate 2 °C.min^{-1}) under vacuum (around 10^{-5} Torr) for 1 hour in the IR cell connected to the vacuum apparatus. Pyridine and collidine adsorption were conducted at 150 °C. After establishing a pressure of 1 Torr at the equilibrium of each adsorbate, the cell was evacuated at 150 °C for pyridine, and at 100 °C for collidine to remove all physisorbed species.

Adsorption and coadsorption of ethanol and/or water:

The adsorption of water and ethanol, as well as their coadsorption at different relative pressures on MFI and MFI@Polymer, were performed using the AGIR technique[39, 40]. It couples the gravimetric analysis with IR spectroscopy to determine simultaneously the quantity of the adsorbed water and/or ethanol. The experiments were carried out on self-supported pellets (~ 20 mg, S = 2 cm^2) and the samples were activated at 150 °C under a gas mixture of argon and oxygen (20 %) at 20 cm^3.min^{-1}. The IR spectra were collected (64 scans at a resolution of 4 cm $^{-1}$, in the spectral region between 600 cm^{-1} and 6000 cm^{-1}) using a Nicolet 6700 spectrometer outfitted with liquid nitrogen cooled MCT detector (mercury, cadmium, and tellurium detector). The mass of the sample and the corresponding spectra were recorded after reaching the equilibrium for each H_2O, EtOH, or H_2O/EtOH concentration. The stability at the

equilibrium was detected by the absence of a change in the sample mass and in the intensity of the characteristic bands of ethanol (at 880 cm^{-1}) and/or water (at 5275 cm^{-1}). Additionally, the outlet flow was monitored by a mass spectrophotometer (Pfeiffer Omnistar GSD301) to ensure the steady state of H_2O and EtOH in the gas phase.

RESULTS AND DISCUSSION

Grafting of SPI-1:

UV-Vis and FTIR spectroscopies:

SPI-1 was grafted on the surface of MFI zeolites via strong covalent interactions. The procedure is described in the experimental part. After grafting the SPI-1 on the surface of the MFI zeolites (SPI-MFI), the obtained samples are characterized by UV-Vis and *in-situ* transmission IR spectroscopies and compared to the MFI parent (**Figure 1**). The UV-Vis of the grafted zeolite (spectrum (b) in **Figure 1(A)**) displays new bands situated between 225 and 300 nm and at 325 nm, not observed for the parent zeolite (spectrum (a)). These bands are attributed to the $\pi - \pi^*$ (225- 300 nm) and $n - \pi^*$(325 nm) electronic transitions of the benzoyl groups of the SPI-1 structure [41].

The reported IR spectrum in **Figure 1(B)** of the SPI-MFI (spectrum (b)) displays the main characteristic bands of SPI-1: $\nu_{(CH)}$ in the 3040-2700 cm^{-1}, $\nu_{(CO)}$ at 1667 cm^{-1}, $\nu_{(CC)}$ between 1580 and 1600 cm^{-1} and 1500-1350 cm^{-1} range assigned to the C=C stretching and CH deformation modes, respectively[42]. The IR spectrum of MFI zeolite (**Figure 1(B)** spectrum (a)) displays $\nu_{(OH)}$ bands at 3743 and 3610 cm^{-1} attributed to silanol located on the outer crystallite surface and to structural bridged SiO(H)Al group respectively. The band at 3743 cm^{-1} totally disappears after grafting whereas the intensity of the bridged structural OH group (3610 cm^{-1}) is hardly affected. This shows that the interactions between the zeolite and the SPI-1 are located on the outer surface of the crystallite [43,44], without affecting significantly the bridging OH groups. The

decrease of the relative intensity of the bands -CH_3 at 2971 cm^{-1} and 1391 cm^{-1} respectively in the subtraction spectrum of SPI-MFI and MFI (**Figure S2**), validates also the grafting procedure through the ethoxy groups of the SPI structure.

Thermogravimetric analysis:

After grafting the silane-based photoinitiator SPI-1 on the surface of the MFI zeolites, the samples are subjected to thermogravimetric analyses (TGA) to determine the quantity of the grafted SPI-1 and to examine its thermal stability. The TG curves and their corresponding dTG curves (**Figure 1(C) and (D)**) reveal a first weight loss below 200 °C (at around 73 °C) for the two samples, which is attributed to the desorption of molecular water. The second weight loss in the SPI-MFI sample starting 180 °C to 800 °C with two peaks at 224 °C and 519 °C corresponds to the thermal degradation of the SPI-1 hydrocarbon. The total weight loss (around 9 wt.%) observed for the SPI-MFI sample is due to the loss of water (around 3 ±1 wt. %) and of SPI-1, which is estimated to be around 6 ±1 wt.%. The thermal stability of the SPI-1 structure is also investigated by IR spectroscopy under vacuum (10^{-6} torr). The evolution of the characteristic vibrational bands of the SPI attributed to the $\nu_{(CH)}$ at different temperatures are reported in **Figure S3**. The results show a high thermal stability up to 180 °C with a low amount of physisorbed species (around 10 % of the total SPI quantity), which agree with the TG results.

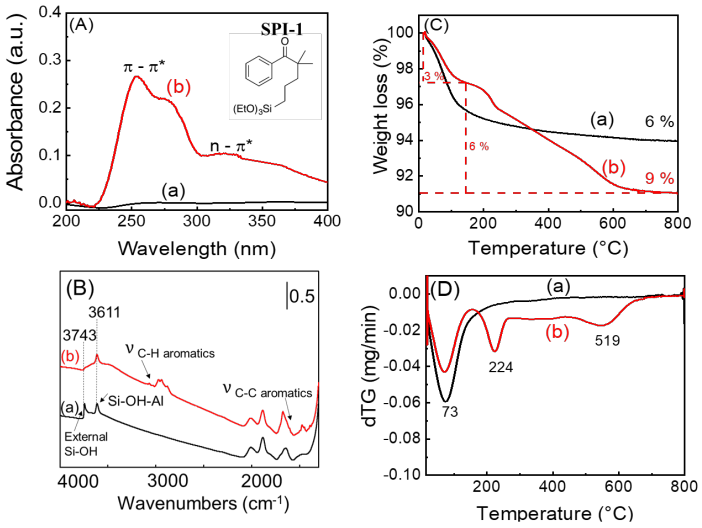

Figure 1: (A) UV-Vis and (B) FTIR spectra, (C) Thermogravimetric curves and (D) dTG of MFI ((a)- black) and SPI-MFI ((b)-red). The samples are activated at 150 °C before recording the IR spectra at RT. Inset (A): chemical structure of SPI-1.

The efficiency of the grafted SPI-MFI in the photopolymerization of TMPA:

A photopolymerization kinetic study is performed thereafter to test the efficiency of the grafted SPI-1 on the MFI surface in the TMPTA photopolymerization under polychromatic and monochromatic (365 nm) irradiations conditions (**Figure 2(A)** and **Figure 2(B)**, respectively). The evolution of the C=C of the TMPTA monomer is studied for SPI-1 (1wt%, **curve (a)**) and for 20 wt. % SPI-MFI (**curve (b)**). Freestanding polymer films are obtained for both samples under polychromatic UV irradiations.

Under polychromatic UV irradiation (**Figure 2(A)**), a decrease of around 20% in the conversion yield is observed when SPI-1 is grafted, which can be attributed to the shading effect of the inorganic filler on the absorbance of the SPI-1. On the other hand, under monochromatic irradiation (**Figure 2(B)**), the conversion yield of the SPI dispersed in the monomer (curve (a)) (around 30 %) is lower than that obtained under polychromatic irradiation (around 55 %) attributed to a low absorption of SPI at 365 nm. This explains the choice of the

polychromatic irradiation in further experiments. Similar behavior is observed for 20 and 30 wt.% SPI-MFI under monochromatic and polychromatic irradiations: a decrease in the C=C conversion yield compared to the pure SPI and an induction time of 20 seconds are observed under 365nm. This might be explained by the fact that the quantity of the quenchers is greater than that of the radicals in such irradiation conditions. As a conclusion, despite the impact of the zeolite on efficiency of the grafted SPI-1, this later still shows a high photopolymerization capacity under polychromatic irradiation, and the optimal filler:monomer ratio is around 1:2.

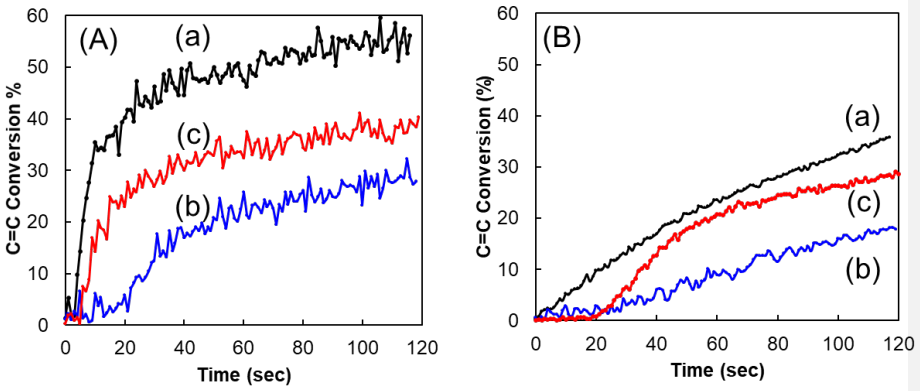

Figure 2: Photopolymerization of trimethylolpropane triacrylate (TMPTA) under (A) polychromatic UV (Hg-Xe lamp) and (B) 365 nm (LED) irradiation using (a) 1 wt.% of SPI-1, (b) 20 wt.% of SPI-MFI and (c) 30 wt.% of SPI-MFI (correspond to 1.2 and 1.8 wt.% of SPI-1 equivalent, respectively). Photopolymerization condition: photopolymerization realized in laminated (air-free) condition (100 μm of thickness).

***Preparation and characterization of MFI@Polymer hybrid materials*:**

Based on the previous results, the preparation of the MFI@Polymer was performed by dispersing MFI-SPI in TMPTA/AcN solution under Ar atmosphere and polychromatic irradiation (**Figure 3(A)**). More details on the preparation of the hybrid materials can be found in the experimental part. After purification, the obtained MFI@Polymer powder is subjected

to different characterization techniques including TGA, UV-Vis, and IR spectroscopy. The experiment was repeated several times and the error was estimated at around 10%.

Polymer loading in the MFI@Polymer hybrid material:

The sample is subjected to IR spectroscopy to investigate the formation of the polymer. The IR spectrum in **Figure 3(B)** of the MFI@Polymer (spectrum (b)) shows the characteristic bands of the CH_2- and CH_3- groups of the polymer in the spectral region between 3040-2700 cm^{-1} and 1350-1480 cm^{-1} corresponding to the $\nu_{(C\text{-}H)}$ and $\delta_{(C\text{-}H)}$ respectively, the $\nu_{(C\text{-}C)}$ of the alkene groups between 1650 cm^{-1} and 1540 cm^{-1} as well as the $\nu_{(C=O)}$ at 1736 cm^{-1}. However, the relative intensity of the $\nu_{C=C}$ band at 1650 cm^{-1} is very low confirming the high articulation of the polymers and the low content of terminal and unpolymerized function.

The TG curves of the grafted SPI-MFI and the prepared sample (MFI@Polymer), as well as the corresponding dTG curves, are represented **in Figure 3(B) and (C).** Similarly to the TG curve of SPI-MFI **(Figure 3 (B) curve (a)**), the TG curve of MFI@Polymer (**Figure 3(B) curve (b)**) reveals a first weight loss (around 4 wt.%) below 200 °C, attributed to the water desorption. Above 200 °C, the chemical and physical degradations of the polymer structure start as well as the degradation of the remaining anchoring group of the SPI-1. These degradations are determined at the two-weight losses observed at 412 °C and 519 °C. The total weight loss is calculated around 44 wt.%. The quantity of the hydrocarbon loading in the MFI@Polymer sample is then determined to be around 40 ± 4wt.% (error estimated on three independent experiments). This result reveals a high polymer loading if we consider the low mass density of the hydrocarbon in respect to the filler (2 to 3 times lower than that of MFI).

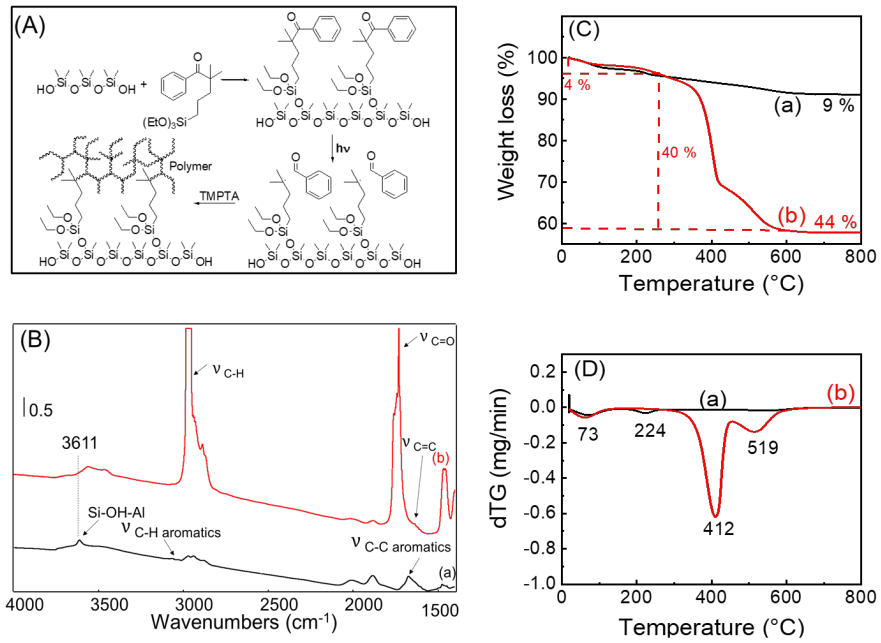

Figure 3: (A) Scheme of photopolymerization, (B) FTIR spectra, (C) thermogravimetric curves, and (D) dTG of SPI-MFI ((a)- black) and MFI@Polymer ((b)-red). The samples are activated at 150 °C before recording the IR spectra at RT.

Structural and textural properties:

After confirming the grafting and the polymerization processes, the crystal structure of the zeolite is examined using powder X-ray diffraction analysis. The PXRD patterns in **Figure 4(A)** indicate the preservation of the zeolite crystallinity after both grafting and photopolymerization processes.

Moreover, the porosity of synthesized hybrid materials is investigated using N_2 sorption at 77 K. The choice of the degassing temperature was made after a study conducted on MFI@Polymer at three different degassing temperatures: 150 °C, 180 °C, and 200 °C. The N_2 adsorption/desorption isotherms are represented in **Figure S4** and **Table S1**. They show a significant decrease of the micropore volumes with the increase of the temperature. This

decrease could be explained by the physical change of the polymer with the increase of the temperature, making the polymers denser with the temperature around the zeolite particles and blocking partially the accessibility to the pores. Therefore, in all the coming experiments the activation temperature, when needed, is set at 150 °C. The N_2 isotherms at 77 K of MFI, SPI-MFI, MFI@Polymer and Polymer are represented in **Figure 4(B)** and the corresponding NLDFT cumulative pore volumes are shown in **Figure S5**. The micropore volumes, the surface areas deduced from BET analysis, and the t-plot method are summarized in **Table 1**. The measurements were conducted several times to ensure the reproducibility of the obtained results.

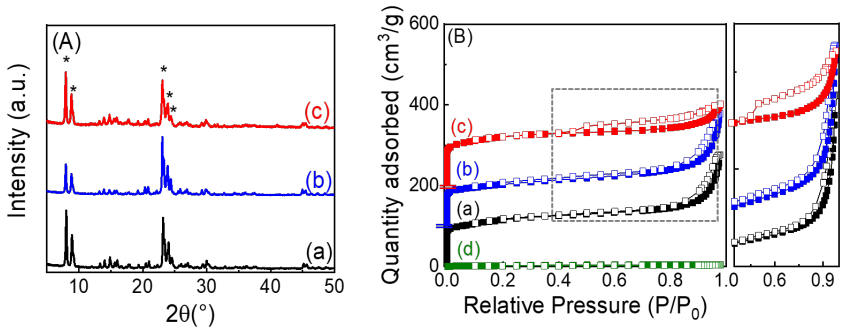

Figure 4: (A) PXRD patterns and (B) N_2 adsorption/desorption isotherms at 77 K of MFI ((a)-black), SPI-MFI ((b)- blue), MFI@Polymer ((c)- red)) and Polymer ((d)-green). The inset of (B) corresponds to zooming on the region of P/P_0 between 0.4 and 1. The adsorption/desorption isotherms of SPI-MFI ((b)) and MFI@Polymer ((c)) are offset vertically for clarification of 100 and 200 cm^3/g, respectively.

It is worthwhile noticing that the SPI grafting and then the polymerization processes did not affect significantly the micropore volume of the MFI zeolites since more than 90 % of the micropore volume is preserved for MFI@Polymer material. This confirms that the polymerization occurs on the outer surface of the crystallite without affecting the accessibility of N_2 towards the zeolite micropores. By contrast, the external surface area significantly

increases after polymerization suggesting that the polymerization process generates a supplementary mesoporosity confirmed by the presence of a H4-type hysteresis loop[45]. Of particular interest, for the MFI@Polymer, a sharp closure of the hysteresis loop is observed at P/P_0 = 0.4-0.5 during the desorption. This behavior is directly related with the so-called cavitation phenomena indicating that a substantial fraction of the pores only have access to the outer surface via opening/necks being smaller than ~ 5 nm, being very characteristic of core-shell materials[46] made from a mesoporous polymeric structure on the MFI zeolite,. Additionally, the comparison between the NLDFT cumulative pore volumes of the MFI and MFI@Polymer (**Figure S5**) reveals no difference in the volume distribution between the two samples at small pore width (below 10 nm), confirming that the polymer grafting happens only on the external surface of the zeolites. The absence of the microporosity in the pure polymer confirms also that the microporosity in the hybrid material is solely coming from the core zeolites and is still accessible after the polymerization process. Considering the hydrocarbon content in SPI-MFI and MFI@Polymer, we can assume that the microporosity of the zeolite is highly preserved after both grafting and photopolymerization processes. The non-significant decreases of the porosity in both cases can be assigned to the covering/poisoning of the external acid sites or to a partial blockage of the porosity (lower than 20%). Further investigation of the samples' acidity will be presented later in this paper.

Table 1: Textural properties of MFI, SPI-MFI, MFI@Polymer, and Polymer tested by N_2 adsorption/desorption at 77 K.

	MFI	**SPI-MFI**	**MFI@Polymer**	**Polymer**
S_{BET} [a] (m^2/g)	413	378 * (355)	402 ** (241)	0
External surface area [b] (m^2/g)	83	101 * (95)	232 ** (139)	9
Total Volume (cm^3/g)	0.420	0.415 * (0.390)	0.312 ** (0.187)	< 0.01
Micropore volume [c] (cm^3/g)	0.145	0.120 * (0.113)	0.133 ** (0.08)	0

[a] BET surface area, [b,c] *t*-plot. The represented values between parentheses are the raw values, without normalization to the mass of zeolite. Values with * and that with ** are normalized to the same mass of zeolite (94 %) and (60 %) respectively, based on the TG results.

Morphological characterization:

The morphology of the MFI zeolites and the MFI@Polymer samples is then examined using scanning electron microscopy (SEM) and transmission electron microscopy (TEM) (**Figure 5**). The images in **Figure 5((A)** and **(C))** show that the pure zeolite sample is formed of agglomerated nanospheres of around 30-50 nm. After the photopolymerization process, these nanocrystals are covered by an opaque layer of the polymer **(Figure 5(B)** and **(D))**. The SEM images didn't reveal the presence of any isolated polymer particles.

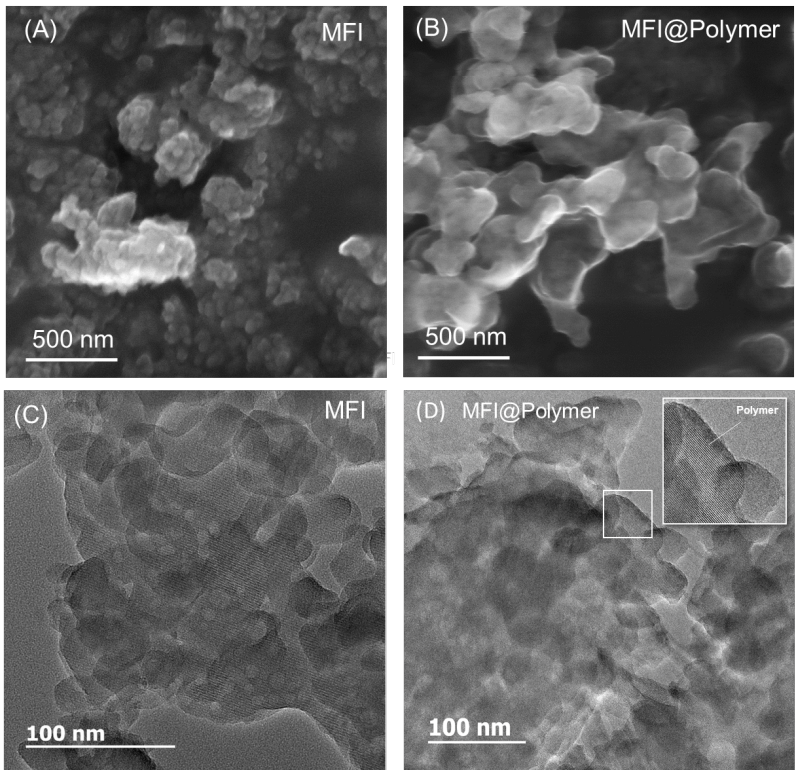

Figure 5: SEM images (A and B) and TEM images (C and D) of MFI ((A) and (C)) and MFI@Polymer ((B) and (D)). The inset of (D) corresponds to a zooming on the polymer layer at the edge of the zeolites.

Commented [ZR1]: change of numbering from A1-A2… to A-B-C-D

The TEM micrographs (**Figure 5 (D)**) confirm this coverage where darker regions are observed at the edge of the crystalline network of the MFI zeolite particles. A multiple core-shell like-structure can be observed, where MFI zeolites are covered by an external shell layer of polymer. This structure can be clearly noticed using elemental analysis EDX coupled to both SEM and TEM. The micrographs in **Figure 6** (and **Figures S6-S9** in SI) show the distribution of Si, O, and C atoms. The latter one is highly condensed on the edge of the particles whereas Si and O are homogeneously distributed. The results confirm a selective and homogeneous distribution of the polymers around the zeolites particles.

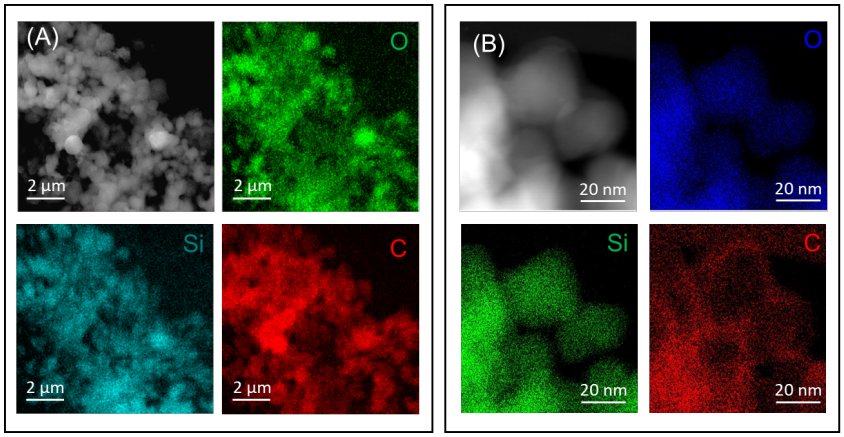

Figure 6: (A) SEM image with EDX (O: green, Si: blue, C: red; scale = 2 μm) and (B) TEM images with EDX (O: blue, Si: green, C: red; scale = 50 and 20 nm) of MFI@Polymer.

Accessibility of the acid sites of the MFI in MFI@Polymer:

The accessibility of the acid sites of MFI zeolites (BAS (SiOHAl)), before (MFI) and after grafting (SPI-MFI) and polymerization (MFI@Polymer), is estimated upon adsorption of probe molecules: (i) pyridine that can be protonated by both internal and external acid sites and (ii) collidine, that specifically interacts with the external surface sites due to steric hindrance[42, 47]. The resulting IR spectra are displayed in **Figure 7** and correspond to the regions of the characteristic bands of each probe molecule. The band at 1547 cm^{-1} in **Figure 7(A)** is attributed to the pyridinium ions interacting with the BAS [48]. For collidine, the bands situated at 1637-1645 cm^{-1} are characteristic of collidinium ions [49] (**Figure 7(B)**). The amount of adsorbed pyridinium and collidinium formed on the acidic sites was determined by integrating the area of their characteristic bands and using the following molar absorption coefficients: $\varepsilon_{1547} = 1.13\ \text{cm.}\,\mu\text{mol}^{-1}$ [50], and $\varepsilon_{1637} = 10.1\ \text{cm.}\,\mu\text{mol}^{-1}$[49], respectively.

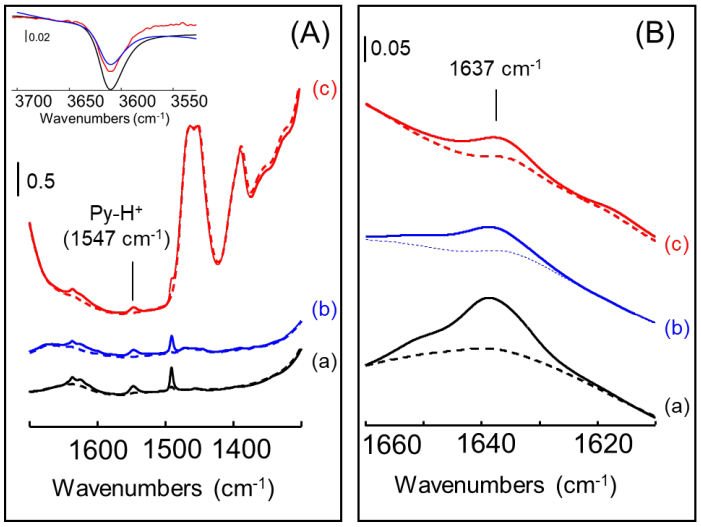

Figure 7: IR spectra of MFI ((a)- black), SPI-MFI ((b)- blue) and MFI@Polymer ((c)-red) before (dotted line) and after (solid line) (A) pyridine and (B) collidine adsorption. The inset of (A) corresponds to the subtraction spectra in the OH region. The spectra are collected after pyridine adsorption at 150 °C and after collidine adsorption at 100 °C and are normalized to the mass of the pellet (20 mg) and the mass of zeolite in each sample. The samples were previously degassed under vacuum at 150 °C.

The amount of BAS accessible to the two probe molecules in the three different samples are summarized in **Table 2.** The comparison of the amount of pyridinium (216 μmol. g^{-1}) and collidinium species (17 μmol. g^{-1}) detected on MFI shows that the proportion of Bronsted acid site located on the external surface is relatively low, about 9 % of the total number of BAS. The comparison of the amount of pyridinium detected on the three materials clearly shows that more than 90 % of the Bronsted acid site remains accessible to pyridine molecules after both SPI-1 grafting and polymerization. Interestingly, these results agree with the preservation of the microporous volume determined by the N_2 sorption experiment. This demonstrates that the encapsulation method used in the present study conserved the Bronsted acidity of the core material in addition to the high permeability of the polymer towards pyridine.

The decrease of about 10 % of the total number of BAS in SPI-MFI and MFI@Polymer is mainly attributed to the significant decrease in the proportion of external Bronsted acid sites (more than 50 %). This is due to the poisoning or the disappearing of the outer BAS resulting from the grafting of the SPI-1 on the outer surface of the zeolite.

Table 2: Accessibility of MFI, SPI-MFI, and MFI@Polymer tested by adsorption of pyridine and collidine.

	MFI	**SPI-MFI**	**MFI@Polymer**
n(μmol/g) Pyridine	216 (100 %)	187 * (93 %)	197 ** (92 %)
n(μmol/g) Collidine	17 (100 %)	7 * (43 %)	9 ** (54 %)

The represented values with * and that with ** are normalized to the mass of zeolite (94 %) and (60 %), calculated by TG, respectively. The values between parentheses correspond to the percentage of the accessible sites compared to the parent zeolite.

Coadsorption of ethanol/water mixture on MFI and MFI@Polymer hybrid materials:

Water and ethanol adsorption capacities of MFI and MFI@Polymer:

After successfully synthesizing, characterizing the hybrid materials, and confirming the accessibility to the pores of the zeolites, the adsorption and separation capacities of the synthesized core-shell materials are tested for water, ethanol, and for ethanol/water mixture using the AGIR instrument. The evolution of the characteristic bands of ethanol at 880 cm^{-1} attributed to the C-C-O vibrations (ν_{C-C-O}) and 1450 cm^{-1} (δ_{CH_3}) and that of water at 1630 cm^{-1} (δ_{H_2O}) and the combination band at 5270 cm^{-1} ($(\delta + \nu)_{H_2O}$) was monitored using IR spectroscopy. However, in our case the characteristic band of ethanol at 1450 cm^{-1} (δ_{CH_3}) and that of water at 1630 cm^{-1} cannot be studied in the case of MFI@Polymer, due to their perturbation with a characteristic band of the polymer ($\delta_{(C\text{-}H)}$ and $\nu_{C=C}$, respectively). Since the coupling of the TG with the IR allows quantifying the adsorbed amount and the corresponding

vibrational band area, respectively, the molar adsorption coefficient for the characteristic bands (ε (cm.μmol^{-1})) of ethanol situated at ~880 cm^{-1} and that of water at ~5270 cm^{-1} for MFI and at ~5240 cm^{-1} for MFI@Polymer can be calculated (**Figure S10**). They allow later to determine the exact quantity of the adsorbed species once they are simultaneously present. The shift of the combination band of the molecular water on MFI@Polymer in respect to pure MFI ($\Delta\nu$ = 30 cm^{-1}) could reflect different configurations of adsorbed water and thus explains the difference between the values of the adsorption coefficients of the two materials. This shift might be explained by two hypotheses: the first one is that the external silanols on the zeolites of the MFI@Polymer sample are completely occupied by the polymer. Thus, the remaining active sites for water adsorption are the internal active sites in the pores of the zeolites. The second hypothesis is that the polymer is capable of adsorbing water by H-interactions between its carbonyl functions and water molecules. **Figure 8** shows the gravimetric adsorption isotherms of adsorbed ethanol and water on MFI and MFI@Polymer. The isotherms are determined after measuring the recorded change in mass using the microbalance of the AGIR setup as a function of the increasing partial pressures of each adsorbate. The evolution of the corresponding IR spectra and the rise of the intensities of the corresponding vibrational characteristic bands are represented in **Figure S11.** Upon ethanol adsorption and after normalization to the mass of the zeolite (inset of **Figure 8(A)**), the microporosity of the zeolite in the MFI@Polymer is filled with ethanol, slightly lower than that of MFI. Once the porosity of the zeolite is filled, the remaining ethanol is adsorbed on the mesoporous polymer. Nevertheless, this trend is not observed for water (**Figure 8(B)**). The quantity of the adsorbed water in the zeolite micropores is low compared to the MFI zeolites and is not sufficient to fill its microporosity confirming the presence of a relatively hydrophobic barrier formed by the polymer around the MFI particles. However, the polymer demonstrates a capacity to interact weakly with water at relatively high partial pressure. The comparison between the water and

the ethanol isotherms demonstrate that MFI have a good capacity to adsorb both water and ethanol, however MFI@Polymer's capacity to adsorb ethanol is much higher than that of water. The main adsorption of water at the outer surface (probably via a weak hydrogen bond with the polymer carbonyl function) may explain the observed shift of the water vibration band and the 3 times higher extinction coefficient in respect to MFI. This result suggests the highly desirable behavior of the hybrid MFI@Polymer for ethanol dehydration.

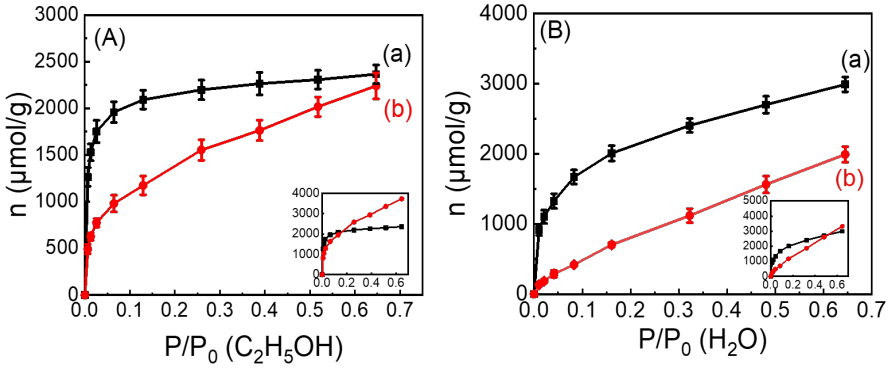

Figure 8: (A) Ethanol and (B) water gravimetric adsorption isotherms on MFI ((a)- black) and MFI@Polymer ((b)- red). The adsorptions were conducted at RT. The insets figures correspond to the adsorbed quantities of ethanol and water after normalization to the mass of zeolite, determined from the TG (60 % of zeolites in the sample MFI@Polymer).

Ethanol /water co-adsorption capacities of MFI and MFI@Polymer:

The coadsorption of ethanol/water mixture at RT is further studied on MFI and MFI@Polymer at a fixed water concentration and increasing ethanol partial pressure. First, a water partial pressure ($P/P_0 = 0.3$, 10000 ppm) is adsorbed on both samples and maintained constant. Once the equilibrium is reached, the gas flow is enriched with an increasing ethanol partial pressure.

The evolution of the IR spectra of MFI and MFI@Polymer during the coadsorption of ethanol/water mixture is represented in **Figure 9((A)-(E))**. Using the previously determined values of the molar adsorption coefficients, the quantities of adsorbed ethanol and water are

calculated from the corresponding IR spectra (**Figure 9(F)**). The initial amount of adsorbed water on the MFI is greater than that adsorbed on MFI@Polymer, which is in accordance with the previous results of the pure adsorption of water. For MFI zeolites, at low ethanol partial pressure ($P/P_0 < 0.1$), water is strongly desorbed. With the increase of the vapor pressure of the ethanol, the quantity of desorbed water is increasing, simultaneously with the increase of the quantity of adsorbed ethanol. At $P/P_0 > 0.3$, the adsorption capacity of the zeolite is reached where a steady state of the amount of ethanol and desorbed water is observed. This might be explained by the high basicity of ethanol compared to H_2O, that is being replaced on the acidic sites of the zeolite. A different trend is observed on MFI@Polymer. At P/P_0 of ethanol < 0.1, weakly adsorbed water molecules are replaced by ethanol. The remaining quantity not accessible for replacement on MFI@Polymer is greater than that on pure MFI (**Figure S12**). Nevertheless, at higher pressures, the quantity of adsorbed H_2O decreases slowly with the fast increase of the quantity of adsorbed ethanol. The residual adsorbed water is retained in the zeolite while ethanol is remained to be adsorbed on the polymer shell even at relatively high partial pressure, contrary to the MFI sample. This adsorption/desorption trend agrees with the previously discussed adsorption isotherms, where the modification of the surface engender higher ethanol adsorption capacity created in the mesoporosity of the polymer. Therefore, using the new synthesis approach it becomes possible to tune the hydrophobic/hydrophilic characters of the hybrid materials without modifying the core part, which can affect their adsorption capacity and their separation behavior.

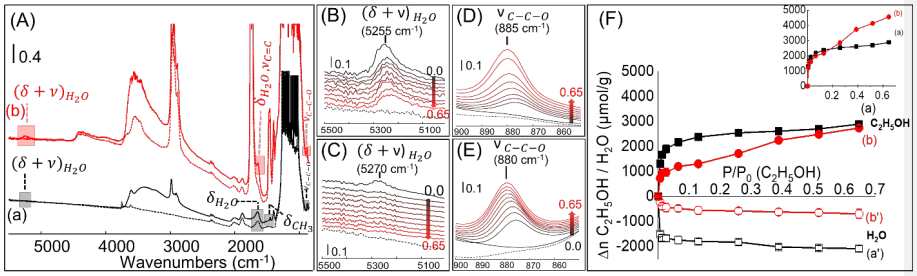

Figure 9: (A) IR spectra of MFI (a) and MFI@Polymer (b) upon adsorption of ethanol/water mixture (P/P_0 C_2H_5OH = 0.013, P/P_0 H_2O = 0.3). Evolution of IR spectra for characteristic bands of water ((B) and (C)) and ethanol ((D) and (E)) upon the coadsorption of ethanol/water mixture with increasing P/P_0 of ethanol from 0 to 0.65 on MFI@Polymer ((B) and ((D)) and MFI ((C) and (E)). The dashed-line spectra correspond to the spectra of the activated sample. (F) Variation of the quantities of adsorbed water ((a') and (b')) and adsorbed ethanol ((a), (b)) on MFI (black) and MFI@Polymer (red) as a function of the partial pressure of ethanol (water concentration in the flow is fixed at 1%). The inset of (F) corresponds to the quantities on MFI@Polymer that are normalized to the mass of zeolite (60% of zeolite). The quantities of the adsorbates are determined from the areas of the characteristic bands of water at 5270 cm^{-1} and ethanol at 880 cm^{-1}.

CONCLUSION

In conclusion, a new synthesis approach of hybrid materials is validated by photopolymerization of TMPTA monomer under UV irradiation as an external shell on the surface of MFI zeolites in the presence of a silane-based photoinitiator (SPI-1). The quantities of the SPI-1 and polymer loading are determined using thermogravimetric analyses. The zeolite-polymer core-shell like structures with homogeneous polymer distribution around the zeolite particles are confirmed by SEM and TEM coupled with EDX. N_2 adsorption/desorption isotherms on the modified material compared to the parent zeolite show that around 90 % of the porosity of the MFI zeolites is still conserved with additional external mesoporosity offered by the polymer, creating thus a hierarchical material. These results are confirmed by adsorption of basic probe molecules. Due to these eminent properties, the hierarchical hybrid materials show a higher capacity to adsorb ethanol with lower capacity to adsorb water in respect to the parent MFI (taking into consideration the zeolite content in both materials). The new approach

opens the way for new classes of hierarchical hybrid materials with tuned hydrophobic/hydrophilic behavior for applications in purification, separation and membranes.

ASSOCIATED CONTENT

Supporting Information: IR spectrum of liquid SPI-1 and compared to the subtraction spectrum between the grafted SPI and MFI, nitrogen adsorption/desorption isotherms at 77K for the three samples degassed at three different temperatures, NLDFT cumulative pore volumes, additional SEM and TEM micrographs with elemental mapping analyses are reported. Areas of the characteristic bands of ethanol and water plotted versus the adsorbed quantities to determine the adsorption coefficients are represented. The evolution of the IR spectra of water and ethanol adsorption, and the quantities of adsorbed water and ethanol during their coadsorption are also reported.

AUTHOR INFORMATION

Corresponding Authors

mohamad.elroz@ensicaen.fr

philippe.bazin@ensicaen.fr

Author Contributions

The manuscript was written through the contributions of all authors. All authors have given approval to the final version of the manuscript.

Funding Sources

This project is financed by European Union (3DZEOPOL project).

Notes

ACKNOWLEDGMENT

Authors acknowledge the Normandy region and European Union for the financial support (3DZEOPOL project). Rita Z.D acknowledges the Normandy region for the doctoral funding.

REFERENCES

1. Ebadi, A.; Mashhadikhan, S.; Sanaeepur, H., Progress in Materials Science Substantial breakthroughs on function-Led design of advanced materials used in mixed matrix membranes (MMMs): A new horizon for efficient CO 2 separation. *Prog. Mater. Sci* **2019,** *102*, 222-295.
2. Jusoh, N.; Yeong, Y. F.; Chew, T. L.; Lau, K. K.; Shariff, A. M., Current development and challenges of mixed matrix membranes for CO2/CH4 separation. *Separation & Purification Reviews* **2016,** *45* (4), 321-344.
3. Dechnik, J.; Gascon, J.; Doonan, C. J.; Janiak, C.; Sumby, C. J., Mixed-matrix membranes. *Angewandte Chemie International Edition* **2017,** *56* (32), 9292-9310.
4. Farnam, M.; bin Mukhtar, H.; bin Mohd Shariff, A., A Review on Glassy and Rubbery Polymeric Membranes for Natural Gas Purification. *ChemBioEng Reviews* **2021**.
5. Castro-Muñoz, R.; Fíla, V., Progress on incorporating zeolites in matrimid® 5218 mixed matrix membranes towards gas separation. *Membranes* **2018,** *8* (2), 30.
6. Gong, H.; Lee, S. S.; Bae, T.-H., Mixed-matrix membranes containing inorganically surface-modified 5A zeolite for enhanced CO2/CH4 separation. *Microporous and Mesoporous Materials* **2017,** *237*, 82-89.
7. Liu, X.; Hu, D.; Li, M.; Zhang, J.; Zhu, Z.; Zeng, G.; Zhang, Y.; Sun, Y., Preparation and characterization of S ilicalite-1/PDMS surface sieving pervaporation membrane for separation of ethanol/water mixture. *Journal of Applied Polymer Science* **2015,** *132* (34).
8. Wu, D.; Han, Y.; Zhao, L.; Salim, W.; Vakharia, V.; Ho, W. W., Scale-up of zeolite-Y/polyethersulfone substrate for composite membrane fabrication in CO2 separation. *Journal of Membrane Science* **2018,** *562*, 56-66.
9. Hasebe, S.; Aoyama, S.; Tanaka, M.; Kawakami, H., CO2 separation of polymer membranes containing silica nanoparticles with gas permeable nano-space. *Journal of Membrane Science* **2017,** *536*, 148-155.
10. Dechnik, J.; Sumby, C. J.; Janiak, C., Enhancing mixed-matrix membrane performance with metal–organic framework additives. *Crystal Growth & Design* **2017,** *17* (8), 4467-4488.
11. Cheng, Y.; Wang, X.; Jia, C.; Wang, Y.; Zhai, L.; Wang, Q.; Zhao, D., Ultrathin mixed matrix membranes containing two-dimensional metal-organic framework nanosheets for efficient CO2/CH4 separation. *Journal of Membrane Science* **2017,** *539*, 213-223.
12. Elrasheedy, A.; Nady, N.; Bassyouni, M.; El-Shazly, A., Metal organic framework based polymer mixed matrix membranes: Review on applications in water purification. *Membranes* **2019,** *9* (7), 88.
13. Kang, Z.; Peng, Y.; Qian, Y.; Yuan, D.; Addicoat, M. A.; Heine, T.; Hu, Z.; Tee, L.; Guo, Z.; Zhao, D., Mixed matrix membranes (MMMs) comprising exfoliated 2D covalent organic frameworks (COFs) for efficient CO2 separation. *Chemistry of Materials* **2016,** *28* (5), 1277-1285.
14. Shan, M.; Seoane, B.; Andres-Garcia, E.; Kapteijn, F.; Gascon, J., Mixed-matrix membranes containing an azine-linked covalent organic framework: Influence of the polymeric matrix on post-combustion CO2-capture. *Journal of Membrane Science* **2018,** *549*, 377-384.

15. Sun, H.; Wang, T.; Xu, Y.; Gao, W.; Li, P.; Niu, Q. J., Fabrication of polyimide and functionalized multi-walled carbon nanotubes mixed matrix membranes by in-situ polymerization for CO2 separation. *Separation and Purification Technology* **2017,** *177*, 327-336.
16. Molki, B.; Aframehr, W. M.; Bagheri, R.; Salimi, J., Mixed matrix membranes of polyurethane with nickel oxide nanoparticles for CO2 gas separation. *Journal of Membrane Science* **2018,** *549*, 588-601.
17. Kononova, S. V.; Gubanova, G. N.; Korytkova, E. N.; Sapegin, D. A.; Setnickova, K.; Petrychkovych, R.; Uchytil, P., Polymer nanocomposite membranes. *Applied Sciences* **2018,** *8* (7), 1181.
18. Vinoba, M.; Bhagiyalakshmi, M.; Alqaheem, Y.; Alomair, A. A.; Pérez, A.; Rana, M. S., Recent progress of fillers in mixed matrix membranes for CO2 separation: A review. *Separation and Purification Technology* **2017,** *188*, 431-450.
19. Hamid, M. R. A.; Jeong, H.-K., Recent advances on mixed-matrix membranes for gas separation: Opportunities and engineering challenges. *Korean Journal of Chemical Engineering* **2018,** *35* (8), 1577-1600.
20. Amooghin, A. E.; Mashhadikhan, S.; Sanaeepur, H.; Moghadassi, A.; Matsuura, T.; Ramakrishna, S., Substantial breakthroughs on function-led design of advanced materials used in mixed matrix membranes (MMMs): a new horizon for efficient CO2 separation. *Progress In Materials Science* **2019,** *102*, 222-295.
21. Galizia, M.; Chi, W. S.; Smith, Z. P.; Merkel, T. C.; Baker, R. W.; Freeman, B. D., 50th anniversary perspective: polymers and mixed matrix membranes for gas and vapor separation: a review and prospective opportunities. *Macromolecules* **2017,** *50* (20), 7809-7843.
22. Maghami, M.; Abdelrasoul, A., Zeolites-mixed-matrix nanofiltration membranes for the next generation of water purification. In *Nanofiltration*, IntechOpen: 2018.
23. Castro-Muñoz, R.; Galiano, F.; Fíla, V.; Drioli, E.; Figoli, A., Mixed matrix membranes (MMMs) for ethanol purification through pervaporation: current state of the art. *Reviews in Chemical Engineering* **2019,** *35* (5), 565-590.
24. Kamelian, F. S.; Mohammadi, T.; Naeimpoor, F., Fast, facile and scalable fabrication of novel microporous silicalite-1/PDMS mixed matrix membranes for efficient ethanol separation by pervaporation. *Separation and Purification Technology* **2019,** *229*, 115820.
25. Wang, S.; Li, X.; Wu, H.; Tian, Z.; Xin, Q.; He, G.; Peng, D.; Chen, S.; Yin, Y.; Jiang, Z., Advances in high permeability polymer-based membrane materials for CO 2 separations. *Energy & Environmental Science* **2016,** *9* (6), 1863-1890.
26. Yang, H.-C.; Hou, J.; Chen, V.; Xu, Z.-K., Surface and interface engineering for organic–inorganic composite membranes. *Journal of Materials Chemistry A* **2016,** *4* (25), 9716-9729.
27. Golemme, G.; Policicchio, A.; Sardella, E.; De Luca, G.; Russo, B.; Liguori, P. F.; Melicchio, A.; Agostino, R. G., Surface modification of molecular sieve fillers for mixed matrix membranes. *Colloids and Surfaces A: Physicochemical and Engineering Aspects* **2018,** *538*, 333-342.
28. Maghami, M.; Abdelrasoul, A., Zeolite mixed matrix membranes (Zeolite-Mmms) for sustainable engineering. *Zeolites and Their Applications; BoD–Books on Demand: Norderstedt, Germany* **2018**, 115.
29. Aroon, M.; Ismail, A.; Matsuura, T.; Montazer-Rahmati, M., Performance studies of mixed matrix membranes for gas separation: A review. *Separation and purification Technology* **2010,** *75* (3), 229-242.
30. Bagheri, A.; Jin, J., Photopolymerization in 3D printing. *ACS Applied Polymer Materials* **2019,** *1* (4), 593-611.

31. Corrigan, N.; Yeow, J.; Judzewitsch, P.; Xu, J.; Boyer, C., Seeing the light: advancing materials chemistry through photopolymerization. *Angewandte Chemie* **2019,** *131* (16), 5224-5243.
32. Douaihy, R. Z.; Telegeiev, I.; Nasrallah, H.; Lebedev, O.; Bazin, P.; Vimont, A.; Chailan, J.-F.; Fahs, A.; Mohamad, E.-R., Synthesis of silica-polymer core-shell hybrid materials with enhanced mechanical properties using a new bifunctional silane-based photoinitiator as coupling agent. *Materials Today Communications* **2021**, 102248.
33. El Roz, M.; Lakhdar, S.; Telegeiev, I. Novel photoinitiators made from bifunctional silane. 2021. *U.S. Patent Application No. 16/764,805*
34. El-Roz, M.; Lalevée, J.; Morlet-Savary, F.; Allonas, X.; Fouassier, J. P., Radical and cationic photopolymerization: New pyrylium and thiopyrylium salt-based photoinitiating systems. *Journal of Polymer Science Part A: Polymer Chemistry* **2008,** *46* (22), 7369-7375.
35. Zhang, Y.; Josien, L.; Salomon, J.-P.; Simon-Masseron, A. l.; Lalevée, J., Photopolymerization of Zeolite/Polymer-Based Composites: Toward 3D and 4D Printing Applications. *ACS Applied Polymer Materials* **2020,** *3* (1), 400-409.
36. Xu, Y.; Jambou, C.; Sun, K.; Lalevée, J.; Simon-Masseron, A. l.; Xiao, P., Effect of zeolite fillers on the photopolymerization kinetics for photocomposites and lithography. *ACS Applied Polymer Materials* **2019,** *1* (11), 2854-2861.
37. Rouquerol, J.; Llewellyn, P.; Rouquerol, F., Is the BET equation applicable to microporous adsorbents. *Stud. Surf. Sci. Catal* **2007,** *160* (07), 49-56.
38. Zholobenko, V.; Freitas, C.; Jendrlin, M.; Bazin, P.; Travert, A.; Thibault-Starzyk, F., Probing the acid sites of zeolites with pyridine: Quantitative AGIR measurements of the molar absorption coefficients. *Journal of Catalysis* **2020,** *385*, 52-60.
39. Bazin, P.; Alenda, A.; Thibault-Starzyk, F., Interaction of water and ammonium in NaHY zeolite as detected by combined IR and gravimetric analysis (AGIR). *Dalton Transactions* **2010,** *39* (36), 8432-8436.
40. El-Roz, M.; Bazin, P.; Birsa Čelič, T.; Zabukovec Logar, N. a.; Thibault-Starzyk, F., Pore Occupancy Changes Water/Ethanol Separation in a Metal–Organic Framework□ Quantitative Map of Coadsorption by IR. *The Journal of Physical Chemistry C* **2015,** *119* (39), 22570-22576.
41. Forbes, W.; Myron, J., Light absorption studies: part XX. The ultraviolet absorption spectra and Infrared carbonyl bands of benzoyl chlorides. *Canadian Journal of Chemistry* **1961,** *39* (12), 2452-2465.
42. Thibault-Starzyk, F.; Vimont, A.; Gilson, J.-P., 2D-COS IR study of coking in xylene isomerisation on H-MFI zeolite. *Catalysis today* **2001,** *70* (1-3), 227-241.
43. El-Roz, M.; Thibault-Starzyk, F.; Wehmeier, A.; Maschke, D.; Blume, A., Silica-silane reaction: Deciphering the silica-silane reaction mechanism for the development of a new generation of low rolling reistsnace tires. *Tire technology international* **2016,** *2016* (43), 93-94.
44. El-Roz, M.; Thibault-Starzyk, F.; Blume, A., Infrared study of the silica/silane reaction. Part II. *KGK Kautschuk, Gummi, Kunststoffe* **2014,** *67* (5), 53-57.
45. Thommes, M.; Kaneko, K.; Neimark, A. V.; Olivier, J. P.; Rodriguez-Reinoso, F.; Rouquerol, J.; Sing, K. S., Physisorption of gases, with special reference to the evaluation of surface area and pore size distribution (IUPAC Technical Report). *Pure and applied chemistry* **2015,** *87* (9-10), 1051-1069.
46. Cychosz, K. A.; Guillet-Nicolas, R.; García-Martínez, J.; Thommes, M., Recent advances in the textural characterization of hierarchically structured nanoporous materials. *Chemical Society Reviews* **2017,** *46* (2), 389-414.
47. Vimont, A.; Thibault-Starzyk, F.; Daturi, M., Analysing and understanding the active site by IR spectroscopy. *Chemical Society Reviews* **2010,** *39* (12), 4928-4950.

48. Vimont, A.; Thibault-Starzyk, F.; Lavalley, J., Infrared spectroscopic study of the acidobasic properties of beta zeolite. *The Journal of Physical Chemistry B* **2000,** *104* (2), 286-291.
49. Nesterenko, N.; Thibault-Starzyk, F.; Montouilliout, V.; Yushchenko, V.; Fernandez, C.; Gilson, J.-P.; Fajula, F.; Ivanova, I., The use of the consecutive adsorption of pyridine bases and carbon monoxide in the IR spectroscopic study of the accessibility of acid sites in microporous/mesoporous materials. *Kinetics and catalysis* **2006,** *47* (1), 40-48.
50. Guisnet, M.; Ayrault, P.; Datka, J., Acid properties of dealuminated mordenites studied by IR spectroscopy. 2. Concentration, acid strength and heterogeneity of OH groups. *Polish journal of chemistry* **1997,** *71* (10), 1455-1461.